# Electric-field-induced generation of spin waves in antiferromagnetic films with voltage-controlled magnetic anisotropy

Alla M. Poletaeva, Andrei I. Nikitchenko, and Nikolay A. Pertsev*
*Ioffe Institute, 194021 St. Petersburg, Russia*

(Received 27 August 2025; revised 12 February 2026; accepted 4 March 2026; published 23 March 2026)

Heterostructures that involve contacting magnetic and dielectric layers may possess a voltage-controlled magnetic anisotropy (VCMA) of interfacial origin. In such heterostructures, spin dynamics can be excited by an electric field created in the dielectric layer, which provides an opportunity for the development of energy-efficient spintronic and magnonic devices. Here, we theoretically describe the generation of spin waves by an electric-field-induced modulation of the interfacial magnetic anisotropy in antiferromagnet-dielectric bilayers. Our approach is based on atomistic simulations of VCMA-driven spin reorientations, which are performed for the (001)-oriented FeRh and $Mn_2Au$ films. It is shown that the sinusoidal variation of VCMA gives rise to the steady precession of spins adjacent to the interface, which induces either evanescent or propagating monochromatic spin waves in the antiferromagnetic film. The amplitude of the generated spin wave strongly depends on the frequency of VCMA oscillations, being maximal at about 33 GHz in the FeRh film and 0.9 THz in the $Mn_2Au$ one. The analysis of simulation data enables us to determine dispersion relations of the propagating spin waves and their decay lengths. Importantly, antiferromagnetic magnons with high frequencies ∼100 GHz and large decay lengths ∼300 nm can be excited in the FeRh/MgO bilayers. Our findings show that the antiferromagnet-dielectric heterostructures possessing VCMA provide the opportunity for an energy-efficient electrical generation of high-frequency spin waves.

DOI: 10.1103/sts8-xtks

## I. INTRODUCTION

An electric field created at the surface of a ferromagnetic metal or its interface with a dielectric material can significantly change the surface/interfacial magnetic anisotropy [1–4]. Such a voltage-controlled magnetic anisotropy (VCMA) plays an important role in the magnetization switching in ferromagnet-dielectric nanostructures, enabling easy current-driven magnetization reversal and even electric-field-induced switching [5–9]. Furthermore, the modulation of the interfacial anisotropy by a radiofrequency voltage applied to the dielectric layer makes it possible to generate coherent magnetization precession [10–12], spin waves [13–15], and magnetoelastic waves [16]. Overall, ferromagnet-dielectric nanostructures having VCMA are promising for the development of electric-field-controlled magnonic and spintronic devices [17–19].

First-principles calculations predict that VCMA should be inherent in certain antiferromagnetic nanostructures as well [20–22], and there are experimental observations supporting this prediction [23,24]. The modeling of an antiferromagnet-oxide nanostructure in the macrospin approximation shows that the application of an ultrashort voltage pulse to an oxide layer could induce picosecond precessional switching of the Néel vector in a nanodisk of a metallic antiferromagnet [25]. A recent theoretical study has also predicted that the modulation of VCMA by an ac voltage provides efficient excitation of resonance modes in easy-axis antiferromagnets [26].

In this paper, we describe the generation of spin waves in antiferromagnet-dielectric nanostructures, where the interfacial magnetic anisotropy is periodically changed by an electric field created in the nonmagnetic dielectric layer. Our approach is based on atomistic simulations of time-dependent spin reorientations, which are driven by the oscillating VCMA in metallic antiferromagnets FeRh and $Mn_2Au$. The exchange interactions between localized magnetic moments in FeRh are described by the simplified effective Hamiltonian [27], while the exchange energy of $Mn_2Au$ takes into account the first four nearest-neighbor interactions between Mn spins, which are quantified by exchange constants predicted by first-principles calculations [28]. By numerically solving the system of the atomistic Landau–Lifshitz–Gilbert (LLG) equations with the effective fields allowing for the exchange interactions between the spins and the interfacial and bulk magnetic anisotropies, we determine the VCMA-driven spin dynamics in the FeRh and $Mn_2Au$ films. Our simulations reveal the excitation of the steady precession of spins at the interface, which gives rise to the emergence of a monochromatic spin wave in the antiferromagnetic film. The wave is evanescent at the excitation frequencies below the relevant resonance frequency of the subsurface antiferromagnetic layer, but becomes a traveling one at higher frequencies. By analyzing simulation data, we determine decay lengths of the traveling antiferromagnetic waves, their dispersion relations, and variations of the wave amplitude with the frequency of the VCMA modulation. It is shown that the precession

*Contact author: pertsev.domain@mail.ioffe.ru

 

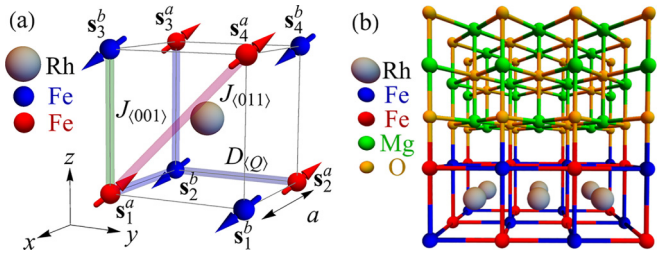


FIG. 1. (a) Atomic structure, exchange interactions, and orientations of magnetic moments in the G-AFM phase of bulk FeRh. (b) Structure of the Fe-terminated FeRh film covered by an MgO nanolayer.

amplitude in the spin wave maximizes near the frequency of the antiferromagnetic resonance occurring in the vicinity of the antiferromagnet-dielectric interface. Analytical dispersion relations derived for magnons propagating in FeRh and $Mn_2Au$ crystals agree with the results of atomistic simulations [29].

## II. ANTIFERROMAGNETIC SPIN WAVES IN FeRh FILMS

The chemically ordered equiatomic FeRh alloy is antiferromagnetic (AFM) below the transition temperature $T_M \approx 350$ K and ferromagnetic (FM) above $T_M$ [30]. Bulk FeRh has a body-centered cubic (bcc-B2) lattice [31], where Fe and Rh atoms are arranged in a checkerboard pattern. In the G-AFM phase stable below $T_M$ [32,33], magnetic moments of the nearest-neighbor Fe atoms are antiparallel [Fig. 1(a)]. Due to the magnetocrystalline anisotropy, Fe moments in bulk FeRh should be collinear with one of the ⟨111⟩ crystallographic directions [34]. Importantly, the G-AFM phase should remain stable in the Fe-terminated FeRh film lattice-matched to MgO [20].

The exchange interactions between magnetic moments in FeRh can be quantified by the simplified effective Hamiltonian

$$H_{\text{eff}} = -\sum_{i,j} J_{ij}\mathbf{s}_i\cdot\mathbf{s}_j + \frac{1}{3}\sum_{i,j,k,l} D_{ijkl}[(\mathbf{s}_i\cdot\mathbf{s}_j)(\mathbf{s}_k\cdot\mathbf{s}_l) + (\mathbf{s}_i\cdot\mathbf{s}_k)(\mathbf{s}_j\cdot\mathbf{s}_l) + (\mathbf{s}_i\cdot\mathbf{s}_l)(\mathbf{s}_k\cdot\mathbf{s}_j)], \quad (1)$$

where the classical spin vectors $\mathbf{s}_i$ of unit length represent the Fe magnetic moments, the first sum describes the Heisenberg exchange interactions including the direct Fe-Fe and indirect Fe-Rh-Fe contributions, and the second sum allows for the four-spin interactions, which involve the Fe-Rh-Fe contributions only [27]. Equation (1) is suitable for the G-AFM phase, in which the magnetic moment of Rh is negligible, while the magnetic moment $\mu_{\text{Fe}}$ of Fe amounts to 3.15 $\mu_B$ [27]. The Heisenberg interactions can be reduced to the nearest-neighbor and next-nearest-neighbor terms defined by the coefficients $J_{\langle 001\rangle}$ and $J_{\langle 011\rangle}$, respectively [Fig. 1(a)]. The four-spin terms can be described by using "basic quartets" of the simple cubic lattice formed by the Fe moments and quantified by the exchange constant $D_{\langle Q\rangle}$ [27]. The three introduced exchange coefficients have been parametrized from the experimental data obtained for the magnetization in the FM phase. The values $J_{\langle 001\rangle} = 0.40\times10^{-21}$ J, $J_{\langle 011\rangle} = 2.75\times10^{-21}$ J, and $D_{\langle Q\rangle} = 0.23\times10^{-21}$ J provide a good agreement with observations [27]. Since an exact Hamiltonian with fully parametrized parameters is not available for FeRh and Eq. (1) satisfactorily describes the observed magnetic behavior of FeRh [27], we used the simplified effective Hamiltonian in our atomistic simulations of spin dynamics in the FeRh films.

An interfacial magnetic anisotropy induced by a dielectric overlayer can be taken into account by adding the term $K_s(\mathbf{s}_i\cdot\mathbf{e}_z)^2$ to the energies of spins $\mathbf{s}_i$ adjacent to the FeRh-dielectric interface, which is assumed to be orthogonal to the $z$ axis of the Cartesian reference frame ($x$, $y$, $z$). For the FeRh/MgO bilayer, the *ab initio* electronic structure calculations predict that the anisotropy parameter $K_s$ depends on the electric field created in the MgO film [20]. Therefore, we performed simulations of the FeRh/MgO nanostructure, focusing on the unstrained FeRh film (lattice constant $a = 0.2995$ nm) with the (001)-oriented Fe-terminated surface, which should exhibit strong variations of $K_s$ with the electric field intensity $E$ [20]. According to the *ab initio* calculations, the interfacial anisotropy $K_s/a^2$ per unit area of the Fe-terminated surface changes from about $+1,6\times10^{-4}\,\text{J m}^{-2}$ at $E = -0.25\,\text{V nm}^{-1}$ to $-2.5\times10^{-4}\,\text{J m}^{-2}$ at the electric field intensity $E = +1\,\text{V nm}^{-1}$ [20]. Hence, at zero field, the interfacial anisotropy favors spin orientations parallel to the interface, whereas at intensities above $E \approx 0.27\,\text{V nm}^{-1}$ it stimulates spin rotations towards directions orthogonal to the interface. Approximating variations of the anisotropy parameter $K_s$ at $E > 0$ by a linear dependence, we obtain the electric-field sensitivity $k_s/a^2 = \partial(K_s/a^2)/\partial E$ of the interfacial anisotropy per unit area to be about $-300\,\text{fJ V}^{-1}\,\text{m}^{-1}$. The magnitude of $k_s/a^2$ is close to the maximum sensitivity of $290\,\text{fJ V}^{-1}\,\text{m}^{-1}$ measured for ultrathin Fe layers on MgO [35]. Converting the aforementioned values into the anisotropy per Fe magnetic moment, we obtain $K_s(E=0) \approx 7.4\times10^{-24}$ J and $k_s \approx -2.7\times10^{-32}\,\text{J V}^{-1}\,\text{m}$.

Using Eq. (1) and adding contributions resulting from the dipolar interactions between the spins and the interfacial and bulk magnetic anisotropies, we obtain the following relation for the complete effective Hamiltonian of the FeRh film:

$$H_{\text{eff}} = -\sum_{i,j} J_{ij}\mathbf{s}_i\cdot\mathbf{s}_j + \frac{D_{\langle Q\rangle}}{3}\sum_{i,j,k,l}[(\mathbf{s}_i\cdot\mathbf{s}_j)(\mathbf{s}_k\cdot\mathbf{s}_l) + (\mathbf{s}_i\cdot\mathbf{s}_k)(\mathbf{s}_j\cdot\mathbf{s}_l) + (\mathbf{s}_i\cdot\mathbf{s}_l)(\mathbf{s}_k\cdot\mathbf{s}_j)] - \mu_{\text{Fe}}\sum_i \mathbf{s}_i\cdot\mathbf{B}_{\text{dip}}(\mathbf{r}_i) + K_b\sum_i[(\mathbf{s}_i\cdot\mathbf{e}_x)^2(\mathbf{s}_i\cdot\mathbf{e}_y)^2 + (\mathbf{s}_i\cdot\mathbf{e}_x)^2(\mathbf{s}_i\cdot\mathbf{e}_z)^2 + (\mathbf{s}_i\cdot\mathbf{e}_y)^2(\mathbf{s}_i\cdot\mathbf{e}_z)^2] + K_s(E)\sum_i(\mathbf{s}_i\cdot\mathbf{e}_z)^2, \quad (2)$$

where the last sum is taken only over the spins $\mathbf{s}_i$ adjacent to the interface. In Eq. (2), $\mathbf{B}_{\text{dip}}(\mathbf{r}_i)$ is the dipolar field at the position $\mathbf{r}_i$ of the spin $\mathbf{s}_i$, which can be calculated by summing magnetic fields created by point dipoles modeling

the Fe magnetic moments. The coefficient $K_b$ defining the cubic magnetocrystalline anisotropy can be extracted from the macroscopic coefficient $K_b/a^3 = -1.35 \times 10^4\,\mathrm{J\,m^{-3}}$ obtained from the measured resonance spectrum of the thick FeRh film grown on MgO [34]. Equation (2) makes it possible to calculate the effective magnetic fields $\mathbf{B}_i^{\mathrm{eff}} = -(1/\mu_{\mathrm{Fe}})\partial H_{\mathrm{eff}}/\partial \mathbf{s}_i$ acting on the spins $\mathbf{s}_i$ in the FeRh film with the interfacial VCMA.

To determine the dynamics of the Fe magnetic moments excited by an ac electric field generated in the MgO overlayer, we numerically solve the system of the atomistic LLG equations

$$\frac{d\mathbf{s}_i}{dt} = -\gamma \mathbf{s}_i \times \mathbf{B}_i^{\mathrm{eff}} + \alpha \mathbf{s}_i \times \frac{d\mathbf{s}_i}{dt}, \tag{3}$$

where $\gamma$ is the gyromagnetic ratio of the Fe atom, and $\alpha$ is the microscopic damping parameter [36]. The solution is based on the numerical integration of Eq. (3) by the projective Runge–Kutta algorithm, which is realized by homemade software developed using the OpenCL framework [37]. We consider the region remote from the lateral boundaries of the antiferromagnetic film, where the spins located in the same plane parallel to the interface should remain collinear during their reorientations. Therefore, the spin dynamics in the films with large in-plane sizes can be calculated in the one-dimensional approximation, which implies the dependence of spin orientations on the perpendicular-to-plane coordinate $z$ only. Each Fe monolayer is modeled by four spins located at the corners of the in-plane square face of the unit cell. The exchange interactions between the nearest and next-nearest neighbors are taken into account via Eq. (1), while the dipolar interactions are neglected because the G-AFM FeRh film has a compensated surface. The damping parameter $\alpha = 4 \times 10^{-3}$ measured at room temperature for the FeRh film grown on MgO(001) [38] is used in our simulations.

The calculations started with the determination of equilibrium spin orientations in thick unstrained FeRh films in the presence of a constant electric field $E_0$ in the MgO overlayer. Since the parameter $K_b$ characterizing the bulk magnetic anisotropy of FeRh is negative [34], far from the interface the Néel vector $\mathbf{L}$ is oriented along one of the $\langle 111 \rangle$ crystallographic directions. This orientation of $\mathbf{L}$ retains up to the interface only at $E_0 \approx 0.27 \times 10^9\,\mathrm{V\,m^{-1}}$ that provides zero $K_s(E_0)$. At other considered field intensities and $E_0 = 0$, the nonzero interfacial anisotropy [20] changes the Néel-vector orientation near the upper surface $z = 0$ of the FeRh film. Hence, the spatial distribution of $\mathbf{L}$ becomes inhomogeneous along the [001] crystallographic direction orthogonal to the interface (Fig. 2). Due to the interfacial anisotropy, the Néel vector $\mathbf{L}(z = 0)$ rotates towards the normal to the FeRh surface at $E_0 = 10^9\,\mathrm{V\,m^{-1}}$, but becomes closer to one of the in-plane $\langle 110 \rangle$ directions at $E_0 = -2.5 \times 10^8\,\mathrm{V\,m^{-1}}$. Remarkably, the calculations of the Néel-vector polar angle $\theta$ show that the influence of the FeRh|MgO interface on spin orientations remains noticeable even at distances $z \sim 100\,\mathrm{nm}$ (Fig. 2).

Simulations of the electrically induced spin dynamics were performed for the sinusoidal modulation $K_s(t) = K_s(E_0) + k_s \delta E_{\max} \sin(2\pi \nu t)$ of the interfacial anisotropy. It was found that such a modulation gives rise to a steady precession of

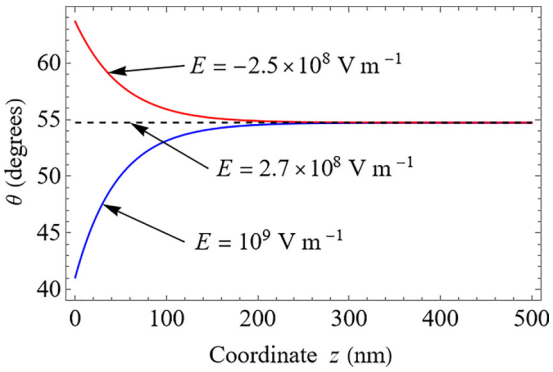


FIG. 2. Equilibrium polar angle $\theta$ of the Néel vector in the FeRh film plotted as a function of the distance $z$ from the interface at different intensities $E$ of the dc electric field in the MgO overlayer.

spins adjacent to the interface. Interestingly, at $K_s(E_0) = 0$ the oppositely oriented spins precess in the same sense (clockwise) when viewed in the spin direction (see Fig. 3), which is similar to the resonance modes in the easy-plane antiferromagnets [39]. By calculating the Néel vector $\mathbf{L}(z = 0, t)$ and magnetization $\mathbf{M}(z = 0, t)$ of the subsurface FeRh layer, we found that $\mathbf{L}$ oscillates in the plane containing its initial [111] direction and the normal to the interface, while $\mathbf{M}$ is parallel to either $[\bar{1}10]$ or $[1\bar{1}0]$ direction orthogonal to the aforementioned plane (Fig. 4). These features of the revealed precession mode can be explained by specific spin rotations, which are induced by the VCMA contribution to the effective fields $\mathbf{B}_i^{\mathrm{eff}}$ involved in Eq. (3). The span $\delta\theta$ of the Néel-vector oscillations varies with the excitation frequency $\nu$ and becomes maximal

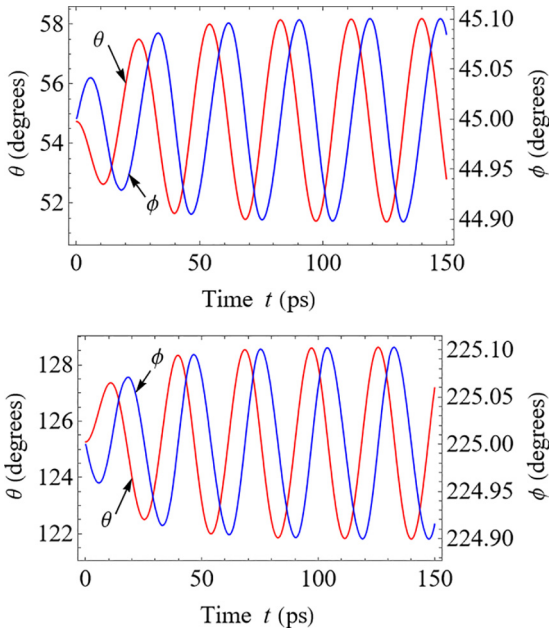


FIG. 3. Time dependences of the azimuth angle $\phi$ and the polar angle $\theta$ characterizing electrically induced precession of subsurface spins in the FeRh film. Two panels show simulation results obtained for the Fe moments having opposite initial directions. The MgO overlayer is subjected to the ac electric field with frequency $\nu = 35$ GHz and amplitude $\delta E_{\max} = 10^8\,\mathrm{V\,m^{-1}}$.

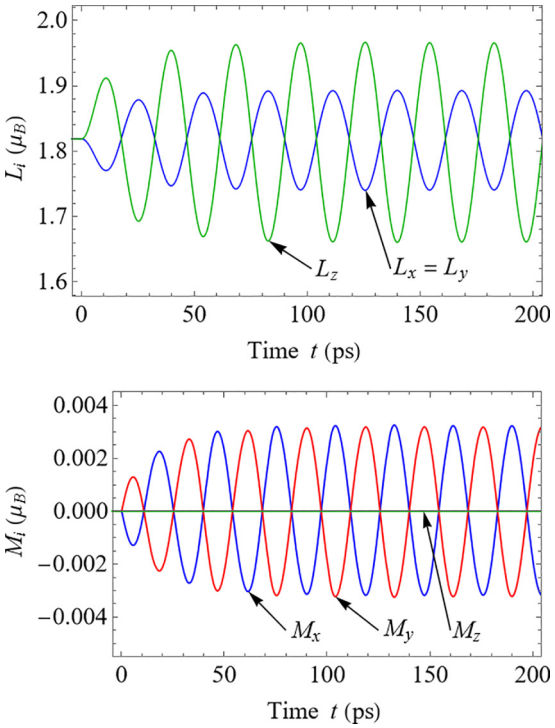


FIG. 4. Electrically induced oscillations of components of the Néel vector **L** and the magnetization **M** in the subsurface FeRh layer. The ac electric field in the MgO overlayer has frequency $\nu = 35$ GHz and amplitude $\delta E_{\max} = 10^8$ V m$^{-1}$.

at $\nu \cong 33$ GHz (see Fig. 5). To clarify the origin of the revealed peak of $\delta\theta(\nu)$, we modeled the relaxation of deflected spins at $E = E_0 = 2.7 \times 10^8$ V m$^{-1}$ to their equilibrium $\langle 111 \rangle$ directions near the interface and determined the resonance frequency $\nu_{\text{res}}$ of the subsurface FeRh region. It was found that $\nu_{\text{res}}$ is close to 33 GHz, which explains the position of the discussed peak.

Our atomistic simulations also revealed that the VCMA-driven precession of Fe moments at the interface gives rise to cooperative spin oscillations inside the FeRh film. At the modulation frequencies below $\nu_{\text{res}}$, these oscillations have the form of evanescent waves. Interestingly, the penetration depths of such waves have large values on the order of

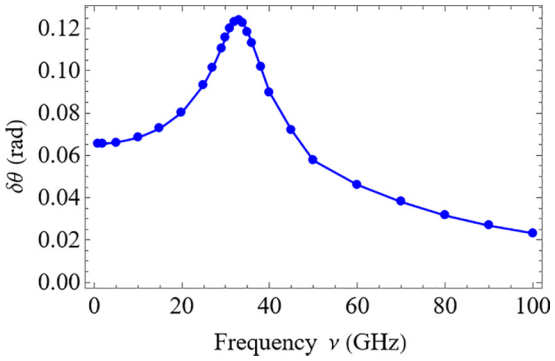


FIG. 5. Maximal span $\delta\theta$ of the polar angle $\theta$ of the electrically induced Néel-vector oscillations in the subsurface FeRh layer plotted as a function of the excitation frequency $\nu$ at $\delta E_{\max} = 10^8$ V m$^{-1}$.

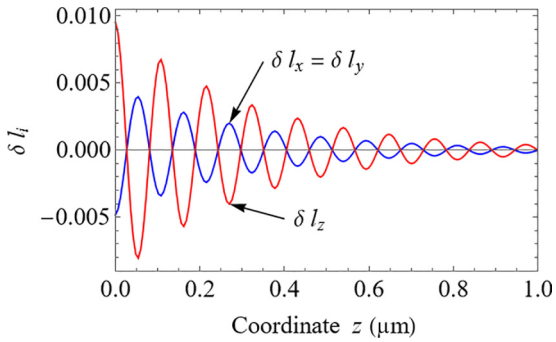


FIG. 6. Antiferromagnetic spin wave generated in the FeRh film at the excitation frequency $\nu = 100$ GHz. The plot shows spatial distributions of changes $\delta l_i$ in the Néel-vector directions cosines at the time $t = 500$ ps. The amplitude $\delta E_{\max}$ of the ac electric field in the MgO overlayer is set equal to $10^8$ V m$^{-1}$.

100 nm (≈200 nm at $\nu = 10$ GHz). This feature correlates with the aforementioned long-range influence of the interfacial anisotropy on equilibrium spin orientations in FeRh. Furthermore, the modulation of $K_s$ at the frequency $\nu > \nu_{\text{res}}$ generates an antiferromagnetic spin wave propagating across the FeRh film (see Fig. 6). Although due to the magnetic damping the spin-wave amplitude exponentially decreases with increasing distance $z$ from the interface, the wave retains significant magnitude even at $z \sim 1$ μm. The decay length $\lambda_{\text{sw}}$ of the spin wave with the frequency $\nu = 100$ GHz is estimated to be about 300 nm.

To determine the dispersion relation $\nu(k)$ of antiferromagnetic spin waves traveling along the [001] crystallographic direction in FeRh, we carried out atomistic simulations at different excitation frequencies and quantified lengths of electrically generated waves. The wave numbers obtained are shown in Fig. 7 together with the resonance frequency $\nu_{\text{res}} = 33$ GHz of the subsurface FeRh region. Importantly, the results of simulations almost perfectly agree with an analytical formula derived in Sec. IV. The spin wave velocity $c_{\text{AFM}} = 10.2 \times 10^3$ m/s is found to be larger than the velocity $c_{\text{AFM}} = 5.9 \times 10^3$ m/s of antiferromagnetic spin waves in NiO [40]. In view of the fact that the resonance frequency of the same mode in NiO is about 240 GHz, this finding looks intriguing.

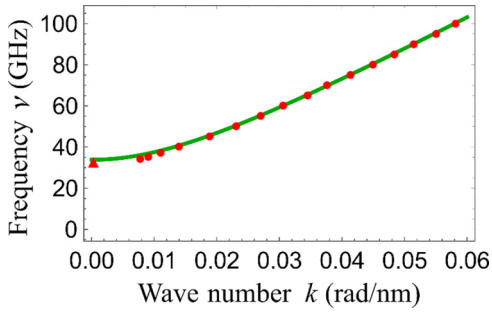


FIG. 7. Dispersion relation of spin waves propagating along the [001] direction in the antiferromagnetic FeRh film. Dots show results of atomistic simulations, while the triangular symbol indicates the numerically determined frequency of antiferromagnetic resonance. The solid line represents the theoretical dispersion relation derived in Sec. IV for antiferromagnetic spin waves in FeRh.

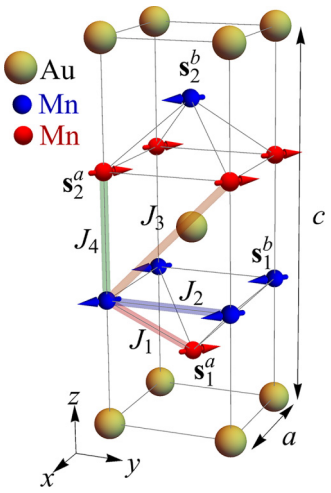


FIG. 8. Atomic structure and orientations of magnetic moments in bulk $Mn_2Au$ having magnetic space group Im'mm.

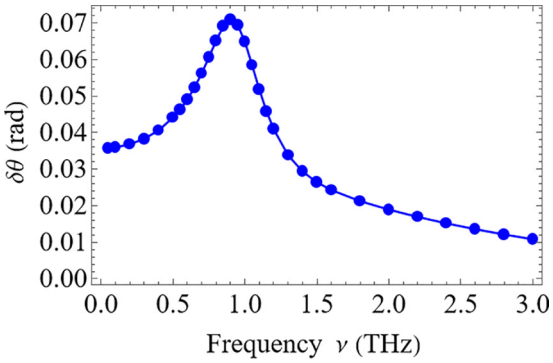


FIG. 9. Maximal span $\delta\theta$ of the polar angle $\theta$ of the electrically induced precession of the Néel vector in the subsurface $Mn_2Au$ layer plotted as a function of the excitation frequency $\nu$.

We explain the higher spin wave velocity and lower resonance frequency in FeRh by the interplay of ferromagnetic (defined by the coefficients $J_{\langle 001\rangle}$ and $J_{\langle 011\rangle}$) and antiferromagnetic ($\propto D_{\langle Q\rangle}$) exchange interactions. Indeed, while the $J_{\langle 001\rangle}$-term weakens the $D_{\langle Q\rangle}$-related antiferromagnetic exchange field for the uniform spin excitations ($k = 0$), the $J_{\langle 011\rangle}$-term drastically increases the exchange energy for magnons with $k \neq 0$. Therefore, the fast spin waves with a relatively low minimal frequency predicted for FeRh are a direct consequence of the ferromagnetic frustration in the G-AFM phase of this alloy.

### III. THz SPIN WAVES IN $Mn_2Au$ FILMS

The metallic antiferromagnet $Mn_2Au$ has a simple spin structure with collinear magnetic moments oriented in the (001) crystallographic plane (Fig. 8) and a high ordering temperature well above 1000 K [41,42]. X-ray and neutron diffraction measurements have shown that bulk $Mn_2Au$ has a tetragonal unit cell and can be assigned the space group I4/mmm [43]. As $Mn_2Au$(001) films can be grown epitaxially [44], we consider the single-crystal tetragonal $Mn_2Au$ film with the (001)-oriented surface. It is assumed that the film is covered by a suitable dielectric material that provides the perpendicular interfacial anisotropy, which can be tuned by an electric field $\mathbf{E}$ created in the dielectric layer. Although the electrical control of the interfacial anisotropy in $Mn_2Au$-dielectric heterostructures has not been confirmed yet, the theoretical predictions of VCMA for antiferromagnetic MnPt and MnPd films [21,22] support the possibility of the supposed control.

To determine the effective fields $\mathbf{B}_i^{\text{eff}}$ involved in the atomistic LLG equations for the unit vectors $\mathbf{s}_i$ defining orientations of the Mn magnetic moments $\mathbf{S}_i = \mu_{\text{Mn}}\,\mathbf{s}_i$, we use the following Hamiltonian $H_i$ of the individual moment $\mathbf{S}_i$ situated at the point $\mathbf{r}_i$:

$$\begin{aligned} H_i = &-\sum_{j\neq i} J_{ij}\mathbf{s}_i\cdot\mathbf{s}_j - \mu_{\text{Mn}}\mathbf{s}_i\cdot\mathbf{B}_{\text{dip}}(\mathbf{r}_i) \\ &+ [K_z + \delta_{ik}K_s(E)](\mathbf{s}_i\cdot\mathbf{e}_z)^2 + K_{zz}(\mathbf{s}_i\cdot\mathbf{e}_z)^4 \\ &+ K_{xy}(\mathbf{s}_i\cdot\mathbf{e}_x)^2(\mathbf{s}_i\cdot\mathbf{e}_y)^2 \end{aligned} \tag{4}$$

where the first term represents the exchange energy between $\mathbf{S}_i$ and the neighboring Mn moments $\mathbf{S}_j$ calculated by the summation over the index $j \neq i$, $K_z = 0.62$ meV, $K_{zz} = 0.024$ meV, and $K_{xy} = -0.058$ meV characterize the magnetocrystalline anisotropy of the tetragonal $Mn_2Au$ [45], $K_s(E)$ is the interfacial anisotropy per Mn moment $\mathbf{S}_k$ adjacent to the $Mn_2Au$-dielectric interface, and $\delta_{ik}$ is the Kronecker delta. The exchange energy of $Mn_2Au$ can be evaluated by summing the first four nearest-neighbor interactions between the Mn moments with $\mu_{\text{Mn}} = 3.87\ \mu_{\text{B}}$ (Fig. 8), which are governed by the exchange constants $J_1 = -5.3422$ mRy, $J_2 = 0.6484$ mRy, $J_3 = -0.6341$ mRy, and $J_4 = -6.8986$ mRy [28]. Using the listed material parameters of $Mn_2Au$, we numerically calculate $\mathbf{B}_i^{\text{eff}} = -(1/\mu_{\text{Mn}})\partial H_i/\partial\mathbf{s}_i$ and employ the obtained data during the solution of the atomistic LLG equations in the one-dimensional approximation. The damping parameter $\alpha$ involved in Eq. (3) is set equal to 0.008 [46].

In simulations of the electric-field-induced spin dynamics, we introduce the sinusoidal modulation $K_s(t) = K_s^0 + \delta K_s \sin(2\pi\nu t)$ of the interfacial anisotropy and assume $K_s^0 = -1.4\times10^{-21}$ J and $\delta K_s = 10^{-23}$ J. The negative value of the zero-field anisotropy parameter $K_s^0$ induces deviation of the Néel vector $\mathbf{L}(z=0)$ at the interface by about 20° from the $\langle 110\rangle$ orientation favored by the bulk magnetocrystalline anisotropy ($\theta \approx 70°$). This out-of-plane deviation gives rise to a nonuniform spatial distribution of $\mathbf{L}$ along the [001] direction orthogonal to the interface, which transforms into almost in-plane spin orientations at distances $z > 10$ nm. The assumed amplitude $\delta K_s$ of the anisotropy modulation is small enough to keep $K_s(t)$ negative at any time and to exclude temporary in-plane orientations of spins located at the interface.

As expected, simulations show that the modulation of the interfacial anisotropy excites coupled oscillations of the Mn magnetic moments adjacent to the interface. These oscillations have the form of the Néel-vector precession around the equilibrium direction, which can be characterized by the maximal span $\delta\theta$ of the polar angle $\theta$ of the vector $\mathbf{L}$. The magnitude of $\delta\theta$ depends on the excitation frequency $\nu$, being significant in the whole studied frequency range $\nu = 50$ GHz–3 THz and reaching maximum at $\nu \approx 0.9$ THz (see Fig. 9). Similar to the spin dynamics in the FeRh film, $\delta\theta(\nu)$ becomes maximal at the excitation frequency $\nu$ close to the resonance frequency $\nu_{\text{res}}$ of the subsurface $Mn_2Au$ layer.

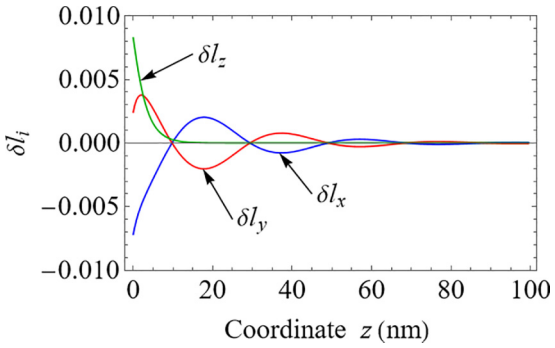


FIG. 10. Antiferromagnetic spin wave generated in the $Mn_2Au$ film at the excitation frequency $\nu = 2$ THz. The plot shows spatial distributions of changes $\delta l_i$ in the Néel-vector directions cosines $l_i$ at the time $t = 10$ ps after the onset of electrically induced spin dynamics.

This conclusion is confirmed by modeling the relaxation of deflected Mn magnetic moments to their equilibrium directions near the interface, which gives $\nu_{\rm res} \approx 0.94$ THz at the chosen value of $K_s^0$.

Due to the exchange interactions, oscillations of the Mn moments at the interface occurring with a frequency $\nu > \nu_{\rm res}$ give rise to an antiferromagnetic spin wave propagating inward the $Mn_2Au$ film. Representative spatial variations of the Néel-vector direction cosines $l_i(z, t)$ in the spin wave with the frequency $\nu = 2$ THz are shown in Fig. 10. The analysis shows that the wave amplitude exponentially decreases with increasing distance $z$ from the interface. The decay length of the spin wave with the frequency $\nu = 2$ THz was found to be about 20 nm.

By performing simulations in a wide range of excitation frequencies and determining wave numbers of the generated spin waves, we evaluated the dispersion relation $\nu(k)$ of the spin waves propagating along the [001] direction in $Mn_2Au$. Figure 11 shows that the dependence $\nu(k)$ becomes practically linear at $k > 0.15$ rad nm$^{-1}$, which agrees with the

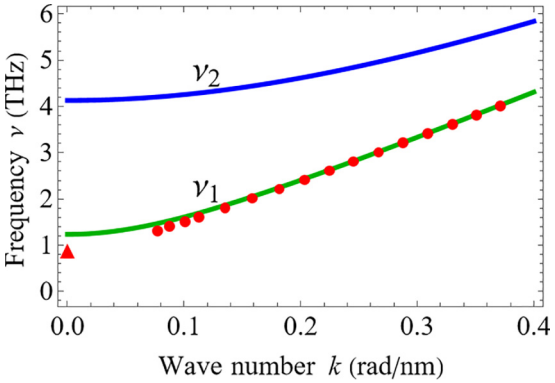


FIG. 11. Dispersion relation of spin waves propagating along the [001] direction in the antiferromagnetic $Mn_2Au$ film. Dots show results of atomistic simulations, while the triangular symbol indicates the numerically determined frequency of antiferromagnetic resonance. The solid lines represent two branches of the theoretical dispersion relation derived in Sec. IV for antiferromagnetic spin waves in $Mn_2Au$.

intermediate behavior of antiferromagnetic spin waves [39]. The simulation data are close to the lower branch of the analytical dispersion relation derived in Sec. IV. Note that the velocity $c_{\rm AFM} = 59.8 \times 10^3$ m/s of the antiferromagnetic spin waves in $Mn_2Au$ is much higher than their velocity $c_{\rm AFM} = 10.2 \times 10^3$ m/s in FeRh. However, the excitation frequencies $\nu$ required to generate such fast magnons in $Mn_2Au$ are well above 1 THz. In contrast, spin waves can propagate in FeRh with their almost maximal velocity already at $\nu \approx 80$ GHz (Fig. 7).

## IV. ANALYTICAL DISPERSION RELATIONS FOR SPIN WAVES IN FeRh AND $Mn_2Au$

To gain more information on antiferromagnetic spin waves propagating in FeRh and $Mn_2Au$ films, we perform analytical calculations of their dispersion relations using atomic-level parameters of exchange interactions. Our calculations are restricted to plane waves, which enables us to employ a one-dimensional approach. We consider only spin waves with small deviations of spin directions from their equilibrium orientations and neglect the Gilbert damping. The dissimilar spin sublattices are represented by the unit vectors $\mathbf{s}_a$ and $\mathbf{s}_b$, which are combined into the magnetic order parameters $\mathbf{m} = (\mathbf{s}_a + \mathbf{s}_b)/2$ and $\mathbf{l} = (\mathbf{s}_a - \mathbf{s}_b)/2$. Accordingly, the atomistic LLG equations given by Eq. (3) are rewritten in the form

$$\frac{d\mathbf{m}}{dt} \approx \frac{\gamma}{2M_s}\left(\mathbf{m} \times \frac{\partial F}{\partial \mathbf{m}} + \mathbf{l} \times \frac{\partial F}{\partial \mathbf{l}}\right), \tag{5}$$

$$\frac{d\mathbf{l}}{dt} \approx \frac{\gamma}{2M_s}\left(\mathbf{l} \times \frac{\partial F}{\partial \mathbf{m}} + \mathbf{m} \times \frac{\partial F}{\partial \mathbf{l}}\right), \tag{6}$$

where $M_s$ is the magnetization of each individual sublattice, and $F$ is the magnetic energy density. We derive explicit expressions for the energy densities $F(\mathbf{m}, \mathbf{l})$ of both FeRh and $Mn_2Au$ and solve the system of Eqs. (5) and (6) for the small-amplitude spin waves propagating along the [001] crystallographic direction.

The crystal structure of FeRh is illustrated in Fig. 1(a), where Fe atoms with the spins $\mathbf{s}_i^a$ and $\mathbf{s}_j^b$ $(i, j = 1, 2, 3, 4)$ and one Rh atom form the cubic unit cell with the size $2a \approx 6$Å. To determine the magnetic order parameters $\mathbf{m}$ and $\mathbf{l}$ of the FeRh monolayer located in the $xy$ plane, it is sufficient to take into account two Fe atoms with the spins $\mathbf{s}_1^a$ and $\mathbf{s}_1^b$. Assuming variations of $\mathbf{m}$ and $\mathbf{l}$ only along the perpendicular $z$ direction and considering all exchange interactions between the spins $\mathbf{s}_i^a$ and $\mathbf{s}_j^b$ and the magnetocrystalline anisotropy defined by Eq. (2), after some mathematical manipulation, we find the magnetic energy density as

$$F = -A_m \mathbf{m}^2 + A_l \mathbf{l} \cdot \frac{\partial^2 \mathbf{l}}{\partial z^2} + \widetilde{K}_b\left(l_x^2 l_y^2 + l_x^2 l_z^2 + l_y^2 l_z^2\right), \tag{7}$$

where $A_m = 2(8D_{\langle Q\rangle} - 3J_{001})/V$, $A_l = a^2(8D_{\langle Q\rangle} - J_{001} + 4J_{011})/(2V)$, $\widetilde{K}_b = K_b/(4V)$, and $V = 8a^3$ is the unit cell volume. Interestingly, despite the peculiar form of the exchange interactions in FeRh [27], which complicates the derivation of $F(\mathbf{m}, \mathbf{l})$, the final expression described by Eq. (7) is quite simple, and its exchange part contains the standard terms proportional to $\mathbf{m}^2$ and $\mathbf{l} \cdot \frac{\partial^2 \mathbf{l}}{\partial z^2}$ only. For small-amplitude spin waves, the cubic magnetocrystalline anisotropy of FeRh can

be replaced by a uniaxial one that favors the Néel-vector orientation along one of the ⟨111⟩ crystallographic axes. In this approximation, we obtain the well-known dispersion relation of an easy-axis antiferromagnet with two degenerate modes [39]:

$$\nu_{1,2} = \frac{\gamma}{4\pi M_s}\sqrt{4K_u A_m + 2A_m A_l k^2}, \tag{8}$$

where $K_u = 2\widetilde{K}_b/3$. Both the resonance frequency $\nu_{\rm res} = \gamma\sqrt{4K_u A_m}/(4\pi M_s) \approx 33.8$ GHz and the high-$k$ spin wave velocity $c_{\rm AFM} = \gamma\sqrt{2A_m A_l}/(2M_s) \approx 10.2 \times 10^3$ m/s are close to the results of our atomistic simulations (see Fig. 7).

The intermetallic compound $Mn_2Au$ has the tetragonal unit cell with the dimensions $a = 3.33$ Å and $c = 8.54$ Å, which involves four Mn atoms with the spins $\mathbf{s}_1^a$, $\mathbf{s}_1^b$, $\mathbf{s}_2^a$, and $\mathbf{s}_2^b$ shown in Fig. 8. In our one-dimensional model, the magnetic state of $Mn_2Au$ can be determined by considering the spins $\mathbf{s}_1^a$ and $\mathbf{s}_1^b$ only, because the spins $\mathbf{s}_2^a$ and $\mathbf{s}_2^b$ of the Mn atoms shifted by the distance $c/2$ along the $z$ axis experience exchange effective fields of the same form. Using Eq. (4), we obtain the following relation for the magnetic energy density of $Mn_2Au$:

$$\begin{aligned} F = & -A_m\mathbf{m}^2 + A_l\mathbf{l}\cdot\frac{\partial^2\mathbf{l}}{\partial z^2} + A_{ml}\mathbf{m}\cdot\frac{\partial\mathbf{l}}{\partial z} + A_{lm}\mathbf{l}\cdot\frac{\partial\mathbf{m}}{\partial z} \\ & + A_{mm}\mathbf{m}\cdot\frac{\partial^2\mathbf{m}}{\partial z^2} + 2\widetilde{K}_{xy}l_x^2 l_y^2 + 2\widetilde{K}_z l_z^2, \end{aligned} \tag{9}$$

where $A_m = 4(4J_1 + 4J_3 + J_4)/V$, $A_l = c^2(4J_3 + J_4)/(2V)$, $A_{ml} = -A_{lm} = -2c(4J_3 + J_4)/V$, $A_{mm} = -c^2(4J_3 + J_4)/(4V)$, $\widetilde{K}_{xy} = 2K_{xy}/V$, $\widetilde{K}_z = 2K_z/V$, and $V = ca^2$ is the unit cell volume (small contribution of the term proportional to $K_{zz}$ is neglected). Next, we write the components of the vectors $\mathbf{m}(z,t)$ and $\mathbf{l}(z,t)$ oscillating with the frequency $\nu$ in the form [47]

$$\begin{aligned} m_x &= -m_y = \delta m_\parallel \exp[i(2\pi\nu t - kz)], \\ m_z &= \delta m_\perp \exp[i(2\pi\nu t - kz)], \\ l_{x,y} &= \frac{1}{\sqrt{2}} \pm \delta l_\parallel \exp[i(2\pi\nu t - kz)], \\ l_z &= \delta l_\perp \exp[i(2\pi\nu t - kz)], \end{aligned} \tag{10}$$

where the complex amplitudes $\delta m_\parallel$, $\delta m_\perp$, $\delta l_\parallel$, and $\delta l_\perp$ of the antiferromagnetic oscillations have absolute values much smaller than unity. The substitution of the above expressions into Eqs. (5) and (6) and the linearization of the latter yields the system of linear equations for the unknowns $\delta m_\parallel$, $\delta m_\perp$, $\delta l_\parallel$, and $\delta l_\perp$, which has the following matrix of coefficients:

$$\begin{pmatrix} \frac{2\pi i\sqrt{2}M_s\nu}{\gamma} & \frac{i}{2}A_{lm}k & 0 & 2\widetilde{K}_z - \widetilde{K}_{xy} - \frac{A_l}{2}k^2 \\ -iA_{lm}k & \frac{2\pi i\sqrt{2}M_s\nu}{\gamma} & A_l k^2 + 4\widetilde{K}_{xy} & 0 \\ 0 & -A_m & \frac{2\pi i\sqrt{2}M_s\nu}{\gamma} & \frac{i}{2}A_{ml}k \\ 2A_m & 0 & iA_{ml}k & \frac{2\pi i\sqrt{2}M_s\nu}{\gamma} \end{pmatrix}, \tag{11}$$

where $\widetilde{K}_{xy} \ll A_m$ is neglected. Setting the determinant of Eq. (11) to zero and solving the equation obtained for the frequency $\nu$, we obtain two branches $\nu_{1,2}(k)$ of the dispersion relation as

$$\begin{aligned} \nu_1 &= \frac{\gamma}{4\pi M_s}\sqrt{8A_m\widetilde{K}_{xy} + \left(2A_m A_l - A_{ml}^2\right)k^2}, \\ \nu_2 &= \frac{\gamma}{4\pi M_s}\sqrt{4A_m(\widetilde{K}_{xy} - 2\widetilde{K}_z) + \left(2A_m A_l - A_{ml}^2\right)k^2}, \end{aligned} \tag{12}$$

where significant simplification is achieved owing to the equality $A_{lm} = -A_{ml}$. The high-$k$ spin wave velocity $c_{\rm AFM} = \frac{\gamma\sqrt{2A_m A_l - A_{ml}^2}}{2M_s} \approx 64.9 \times 10^3$ m/s predicted by Eq. (12) agrees well with the velocity extracted from the results of atomistic simulations (see Fig. 11). As expected for an easy-plane antiferromagnet, the lower branch $\nu_1(k)$ of the dispersion relation corresponds to the Néel-vector precession in the $xy$ plane ($\delta m_\parallel = \delta l_\perp = 0$, $i\delta m_\perp \ll \delta l_\parallel$), while the higher-frequency mode $\nu_2(k)$ describes the oscillation of the vector $\mathbf{l}$ with significant deviations from this plane ($\delta m_\perp = \delta l_\parallel = 0$, $i\delta m_\parallel \ll \delta l_\perp$).

It should be noted that approximate analytical formulae have been derived earlier for the antiferromagnetic resonance frequencies $\nu_{1,2}(k = 0)$ of $Mn_2Au$, but the dispersion relation of this compound has been calculated only numerically in frame of the linear spin-wave theory [48]. Taking into account different types of exchange interactions between the Mn moments and the magnetocrystalline anisotropy, we have extended the analytical approach to the description of spin waves in $Mn_2Au$ and achieved a correct prediction of the high-$k$ spin wave velocity. However, the analytically calculated resonance frequency $\nu_1(k = 0) \approx 1.2$ THz of the bulk $Mn_2Au$ differs significantly from the value of 0.9 THz determined by means of atomistic simulations for the $Mn_2Au$ film with the perpendicular interfacial anisotropy. We attribute this feature to the deviation by about 20° of the Néel-vector equilibrium orientation near the interface from the (001) easy plane of $Mn_2Au$, which weakens the effective field created by the bulk in-plane anisotropy. This explanation is consistent with a difference in the relaxation frequencies determined by atomistic simulations, which yield $\nu_{\rm res} \approx 0.94$ THz at $K_s(t) = -1.4 \times 10^{-21}$ J and $\nu_{\rm res} \approx 1.2$ THz in the absence of the interfacial anisotropy [$K_s(t) = 0$].

Finally, we emphasize the significance of Eqs. (7) and (9) derived for the magnetic energy densities of FeRh and $Mn_2Au$. These relations allow for essential nonlinearities peculiar to inhomogeneous spin dynamics in antiferromagnets, which make them useful for theoretical investigations of large-amplitude spin waves and antiferromagnetic solitons. Despite the importance of four-spin exchange interactions in FeRh [27], the energy density of this compound can be written in the standard form involving only the terms proportional to $\mathbf{m}^2$ and $\mathbf{l}\cdot\frac{\partial^2\mathbf{l}}{\partial z^2}$ and the contribution of magnetocrystalline anisotropy. In contrast, additional terms proportional to $\mathbf{m}\cdot\frac{\partial\mathbf{l}}{\partial z}$ and $\mathbf{l}\cdot\frac{\partial\mathbf{m}}{\partial z}$ significantly influence the characteristics of spin waves in $Mn_2Au$.

## V. CONCLUSION

Performing numerical modeling on the level of individual atomic spins, we quantified the spin dynamics excited in antiferromagnetic films by an alternating electric field created in a dielectric overlayer providing tunable

interfacial anisotropy. Simulations were done for the (001)-oriented FeRh and $Mn_2Au$ films, where the directions of spins adjacent to the antiferromagnet-dielectric interface are inclined to the film surface, which makes them sensitive to variations of the interfacial anisotropy. In FeRh, inclined initial orientations are provided by the bulk magnetocrystalline anisotropy favoring the ⟨111⟩ spin directions [34]. Since the bulk anisotropy of $Mn_2Au$ facilitates the ⟨110⟩ orientations of spins [44], a perpendicular interfacial anisotropy ensuring inclined spin directions at the film surface was introduced for a $Mn_2Au$-dielectric bilayer.

The numerical solution of the system of the atomistic LLG equations showed that the sinusoidal modulation of the interfacial anisotropy generates a steady precession of the Néel vector near the interface. The precession amplitude strongly depends on the modulation frequency $\nu$ and becomes maximal near the relevant resonance frequency $\nu_{res}$ of the subsurface antiferromagnetic layer, for which supplemental simulations give the values of about 33 GHz (FeRh film) and 0.9 THz ($Mn_2Au$ film). Due to the exchange interactions between the spins, their subsurface precession launches an antiferromagnetic spin wave propagating away from the interface. At $\nu < \nu_{res}$, the spin wave is evanescent but has a large penetration depth in the FeRh film (about 200 nm at $\nu = 10$ GHz). The traveling spin waves excited at $\nu > \nu_{res}$ are characterized by the dispersion relations shown in Figs. 7 and 11, which include an almost linear relationship between the frequency $\nu$ and the wave number $k$ at 0.03 rad nm$^{-1}$ $< k <$ 0.06 rad nm$^{-1}$ in the case of the FeRh film and at 0.15 rad nm$^{-1}$ $< k <$ 0.35 rad nm$^{-1}$ in the $Mn_2Au$ one. The validity of our theoretical predictions is confirmed by the good agreement of the results of atomistic simulations with the analytical dispersion relations derived for plane spin waves propagating along the [001] direction in FeRh and $Mn_2Au$ crystals.

Owing to the magnetic damping, the spin-wave amplitude exponentially decreases with the distance from the interface. The decay lengths of the waves propagating across the FeRh and $Mn_2Au$ films are calculated to be about 300 nm at 100 −500 GHz and 20 nm at 1–3 THz, respectively. Since in the FeRh films the decay length is rather large, the electric-field-induced excitation of antiferromagnetic magnons in the FeRh/MgO bilayers can be used for an energy-efficient generation and transmission of high-frequency spin signals in magnonic circuits.

## ACKNOWLEDGMENT

A.M.P. and N.A.P. acknowledge financial support from the Russian Science Foundation (Project No. 23-12-00251).

## DATA AVAILABILITY

The data that support the findings of this article are not publicly available upon publication because it is not technically feasible, and/or the cost of preparing, depositing, and hosting the data would be prohibitive within the terms of this research project. The data are available from the authors upon reasonable request.

[1] M. Weisheit, S. Fähler, A. Marty, Y. Souche, C. Poinsignon, and D. Givord, Electric field-induced modification of magnetism in thin-film ferromagnets, Science **315**, 349 (2007).

[2] C.-G. Duan, J. P. Velev, R. F. Sabirianov, Z. Zhu, J. Chu, S. S. Jaswal, and E. Y. Tsymbal, Surface magnetoelectric effect in ferromagnetic metal films, Phys. Rev. Lett. **101**, 137201 (2008).

[3] T. Maruyama, Y. Shiota, T. Nozaki, K. Ohta, N. Toda, M. Mizuguchi, A. A. Tulapurkar, T. Shinjo, M. Shiraishi, S. Mizukami, Y. Ando, and Y. Suzuki, Large voltage-induced magnetic anisotropy change in a few atomic layers of iron, Nat. Nanotech. **4**, 158 (2009).

[4] K. Nakamura, R. Shimabukuro, Y. Fujiwara, T. Akiyama, T. Ito, and A. J. Freeman, Giant modification of the magnetocrystalline anisotropy in transition-metal monolayers by an external electric field, Phys. Rev. Lett. **102**, 187201 (2009).

[5] W.-G. Wang, M. Li, S. Hageman, and C. L. Chien, Electric-field-assisted switching in magnetic tunnel junctions, Nat. Mater. **11**, 64 (2011).

[6] Y. Shiota, T. Nozaki, F. Bonell, S. Murakami, T. Shinjo, and Y. Suzuki, Induction of coherent magnetization switching in a few atomic layers of FeCo using voltage pulses, Nat. Mater. **11**, 39 (2012).

[7] S. Kanai, M. Yamanouchi, S. Ikeda, Y. Nakatani, F. Matsukura, and H. Ohno, Electric field-induced magnetization reversal in a perpendicular-anisotropy CoFeB-MgO magnetic tunnel junction, Appl. Phys. Lett. **101**, 122403 (2012).

[8] N. A. Pertsev, Origin of easy magnetization switching in magnetic tunnel junctions with voltage-controlled interfacial anisotropy, Sci. Rep. **3**, 2757 (2013).

[9] Y. Shao, V. Lopez-Dominguez, N. Davila, Q. Sun, N. Kioussis, J. A. Katine, and P. Khalili Amiri, Sub-volt switching of nanoscale voltage-controlled perpendicular magnetic tunnel junctions, Commun. Mater. **3**, 87 (2022).

[10] T. Nozaki, Y. Shiota, S. Miwa, S. Murakami, F. Bonell, S. Ishibashi, H. Kubota, K. Yakushiji, T. Saruya, A. Fukushima, S. Yuasa, T. Shinjo, and Y. Suzuki, Electric-field-induced ferromagnetic resonance excitation in an ultrathin ferromagnetic metal layer, Nat. Phys. **8**, 491 (2012).

[11] J. Zhu, J. A. Katine, G. E. Rowlands, Y.-J. Chen, Z. Duan, J. G. Alzate, P. Upadhyaya, J. Langer, P. K. Amiri, K. L. Wang, and I. N. Krivorotov, Voltage-induced ferromagnetic resonance in magnetic tunnel junctions, Phys. Rev. Lett. **108**, 197203 (2012).

[12] G. Viaud and N. A. Pertsev, Dynamic converse magnetoelectric effect in ferromagnetic nanostructures with electric-field-dependent interfacial anisotropy, Phys. Rev. B **90**, 064429 (2014).

[13] R. Verba, V. Tiberkevich, I. Krivorotov, and A. Slavin, Parametric excitation of spin waves by voltage-controlled magnetic anisotropy, Phys. Rev. Appl. **1**, 044006 (2014).

[14] B. Rana, Y. Fukuma, K. Miura, H. Takahashi, and Y. Otani, Excitation of coherent propagating spin waves in ultrathin CoFeB film by voltage-controlled magnetic anisotropy, Appl. Phys. Lett. **111**, 052404 (2017).

[15] A. I. Nikitchenko and N. A. Pertsev, Spin-orbit torque control of spin waves in a ferromagnetic waveguide, Phys. Rev. B **104**, 134422 (2021).

[16] A. V. Azovtsev and N. A. Pertsev, Electrically excited magnetoelastic waves and magnetoacoustic resonance in ferromagnetic films with voltage-controlled magnetic anisotropy, Phys. Rev. B **107**, 054418 (2023).

[17] B. Rana and Y. Otani, Towards magnonic devices based on voltage-controlled magnetic anisotropy, Commun. Phys. **2**, 90 (2019).

[18] P. K. Mishra, M. Sravani, A. Bose, and S. Bhuktare, Voltage-controlled magnetic anisotropy-based spintronic devices for magnetic memory applications: Challenges and perspectives, J. Appl. Phys. **135**, 220701 (2024).

[19] B. Rana, Role of voltage-controlled magnetic anisotropy in the recent development of magnonics and spintronics J. Appl. Phys. **136**, 150701 (2024).

[20] G. Zheng, S.-H. Ke, M. Miao, J. Kim, R. Ramesh, and N. Kioussis, Electric field control of magnetization direction across the antiferromagnetic to ferromagnetic transition, Sci. Rep. **7**, 5366 (2017).

[21] Y. Su, M. Li, J. Zhang, J. Hong, and L. You, Voltage-controlled magnetic anisotropy in antiferromagnetic $L1_0$-MnPt and MnPd thin films, J. Magn. Magn. Mater. **505**, 166758 (2020).

[22] P.-H. Chang, W. Fang, T. Ozaki, and K. D. Belashchenko, Voltage-controlled magnetic anisotropy in antiferromagnetic MgO-capped MnPt films, Phys. Rev. Mater. **5**, 054406 (2021).

[23] Y. Wang, X. Zhou, C. Song, Y. Yan, S. Zhou, G. Wang, C. Chen, F. Zeng, and F. Pan, Electrical control of the exchange spring in antiferromagnetic metals, Adv. Mater. **27**, 3196 (2015).

[24] M. Xu, M. Li, P. Khanal, A. Habiboglu, B. Insana, Y. Xiong, T. Peterson, J. C. Myers, D. Ortega, H. Qu, C. L. Chien, W. Zhang, J.-P. Wang, and W. G. Wang, Voltage-controlled antiferromagnetism in magnetic tunnel junctions, Phys. Rev. Lett. **124**, 187701 (2020).

[25] V. Lopez-Dominguez, H. Almasi, and P. Khalili Amiri, Picosecond electric-field-induced switching of antiferromagnets, Phys. Rev. App. **11**, 024019 (2019).

[26] R. Tomasello, R. Verba, V. Lopez-Dominguez, F. Garescì, M. Carpentieri, M. Di Ventra, P. Khalili Amiri, and G. Finocchio, Antiferromagnetic parametric resonance driven by voltage-controlled magnetic anisotropy, Phys. Rev. Appl. **17**, 034004 (2022).

[27] J. Barker and R. W. Chantrell, Higher-order exchange interactions leading to metamagnetism in FeRh, Phys. Rev. B **92**, 094402 (2015).

[28] J. Hirst, U. Atxitia, S. Ruta, J. Jackson, L. Petit, and T. Ostler, Temperature-dependent micromagnetic model of the antiferromagnet $Mn_2Au$: A multiscale approach, Phys. Rev. B **106**, 094402 (2022).

[29] Throughout this paper, the terms "spin wave" and "magnon" are used interchangeably to refer to the coherent magnetic excitations studied via the classical LLG framework.

[30] J. S. Kouvel and C. C. Hartelius, Anomalous magnetic moments and transformations in the ordered alloy FeRh, J. Appl. Phys. **33**, 1343 (1962).

[31] L. J. Swartzendruber, The Fe−Rh (Iron-Rhodium) system, Bull. Alloy Phase Diagrams **5**, 456 (1984).

[32] G. Shirane, R. Nathans, and C. W. Chen, Hyperfine Fields and magnetic moments in the Fe–Rh system, Phys. Rev. **134**, A1547 (1964).

[33] V. L. Moruzzi and P. M. Marcus, Antiferromagnetic-ferromagnetic transition in FeRh, Phys. Rev. B **46**, 2864 (1992).

[34] X. Zhu, Y. Li, Y. Xie, Q. Qiu, C. Cao, X. Hu, W. Xie, T. Shang, Y. Xu, L. Sun, W. Cheng, D. Jiang, and Q. Zhan, Magnetocrystalline anisotropy of epitaxially grown FeRh/MgO(001) films, J. Alloy. Compd. **917**, 165566 (2022).

[35] T. Nozaki, A. Kozioł-Rachwał, W. Skowrónski, V. Zayets, Y. Shiota, S. Tamaru, H. Kubota, A. Fukushima, S. Yuasa, and Y. Suzuki, Large voltage-induced changes in the perpendicular magnetic anisotropy of an MgO-Based tunnel junction with an ultrathin Fe layer, Phys. Rev. Appl. **5**, 044006 (2016).

[36] R. F. L. Evans, W. J. Fan, P. Chureemart, T. A. Ostler, M. O. A. Ellis, and R. W. Chantrell, Atomistic spin model simulations of magnetic nanomaterials, J. Phys.: Condens. Matter **26**, 103202 (2014).

[37] A. M. Poletaeva, A. I. Nikitchenko, and N. A. Pertsev, Néel vector auto-oscillations and reorientations induced by spin-polarized electric currents in antiferromagnetic $Mn_2Au$ nanolayer, SPIN **14**, 2450017 (2024).

[38] S. Mankovsky, S. Polesya, K. Chadova, H. Ebert, J. B. Staunton, T. Gruenbaum, M. A. W. Schoen, C. H. Back, X. Z. Chen, and C. Song, Temperature-dependent transport properties of FeRh, Phys. Rev. B **95**, 155139 (2017).

[39] S. M. Rezende, A. Azevedo, and R. L. Rodríguez-Suárez, Introduction to antiferromagnetic magnons, J. Appl. Phys. **126**, 151101 (2019).

[40] A. V. Azovtsev and N. A. Pertsev, THz and sub-THz antiferromagnetic magnons via magnetoacoustic resonances excited by picosecond strain pulses in NiO, Phys. Rev. Mater. **8**, 044404 (2024).

[41] V. Barthem, C. Colin, H. Mayaffre, M.-H. Julien, and D. Givord, Revealing the properties of $Mn_2Au$ for antiferromagnetic spintronics, Nat. Commun. **4**, 2892 (2013).

[42] S. Khmelevskyi and P. Mohn, Layered antiferromagnetism with high Neel temperature in the intermetallic compound $Mn_2Au$, Appl. Plys. Lett. **93**, 162503 (2008).

[43] P. Wells and J. H. Smith, The structure of $Mn_2Au$ and $Mn_3Au$, Acta Cryst. **A26**, 379 (1970).

[44] S. Yu. Bodnar, L. Šmejkal, I. Turek, T. Jungwirth, O. Gomonay, J. Sinova, A. A. Sapozhnik, H.-J. Elmers, M. Kläui, and M. Jourdan, Writing and reading antiferromagnetic $Mn_2Au$ by Néel spin-orbit torques and large anisotropic magnetoresistance, Nat. Comms. **9**, 348 (2018).

[45] S. Selzer, L. Salemi, A. Deák, E. Simon, L. Szunyogh, P. M. Oppeneer, and U. Nowak, Current-induced switching of antiferromagnetic order in $Mn_2Au$ from first principles, Phys. Rev. B **105**, 174416 (2022).

[46] Y. Behovits, A. L. Chekhov, S. Y. Bodnar, O. Gueckstock, S. Reimers, Y. Lytvynenko, Y. Skourski, M. Wolf, T. Seifert,

O. Gomonay, M. Kläui, M. Jourdan, and T. Kampfrath, Terahertz Néel spin-orbit torques drive nonlinear magnon dynamics in antiferromagnetic $Mn_2Au$, Nat. Commun. **14**, 6038 (2023).

[47] R. M. Dubrovin, A. V. Kimel, and A. K. Zvezdin, Competition between terahertz magnetoelectric and Néel spin-orbit torque driven spin dynamics in metallic antiferromagnets, Phys. Rev. B **112**, 064402 (2025).

[48] M. Weißenhofer, F. Foggetti, U. Nowak, and P. M. Oppeneer, Néel vector switching and terahertz spin-wave excitation in $Mn_2Au$ due to femtosecond spin-transfer torques, Phys. Rev. B **107**, 174424 (2023).